ADVANCED FUNCTIONAL MATERIALS
www.afm-journal.de

Modulating Charge Transport from Thermally Activated to "Band-Like" Through Interfacial Bottom-Up Binding Capability of Bilayer Polymer Dielectrics

Yingshuang Zheng, Hongzhen Lin, Ting Jiang, Dongyang Zhu, Shengli Qi, Wei Li, Liqiang Li, Deyang Ji, and Wenping Hu**

The disordered chain arrangement of polymer dielectrics has complex both internal and external effects on system performance, which generally stimulates the weak acquisition and grain boundaries of vapor-deposited organic small molecule films (VDOSMFs) with thermally activated charge transport. As a result, achieving "band-like" transmission of VDOSMs on polymer dielectrics is attempting to prove to be a major challenge. Three types of bi-polymer dielectrics are developed to modulate charge transport from thermally activated mode to "band-like" transport at the interfacial level. The bottom consisting of a polyimide layer is critical to interfacial modulation, which shows the selectively binding capability with up-dielectric layers to realize the modulation of charge transport, as corroborated by interface characterization and density functional-based tight-binding calculation. The findings provide an effective strategy for modulating the charge transport through polymer dielectric engineering and also recommend a podium to further comprehend the electrical characteristics of small molecules in organic thin-film transistors.

1. Introduction

Organic field-effect transistors (OFETs) are emerging as one of the most viable voltage-driven current sources for a wide range of applications, including OLED backplane drives, flexible wearable electronic devices, and so on.[1–7] In contrast to conventional inorganic semiconductors, where carriers transport in delocalized energy bands as amplitude-modulated plane waves to form high-quality energy band transport,[8] carriers in organic semiconductors are usually in a localized state,[3,4] indicating that achieving band-like transport is still a significant challenge. With the promotion of organic single crystals[9–16] or solution-processed crystalline films,[17–20] it has been discovered that the organized configuration of the molecules causes the molecular thermal lattice vibration to be comparatively weak, resultantly the electron-phonon coupling effect will not damage the charge transport during the temperature reduction process, resulting in the observation of band-like transport in certain organic devices. Only a few cases have been reported in the case of polymer semiconductors[21–23] where the innate disorder in the channel layer could be efficaciously repressed by making adjustments of the main and side chain for a larger transport essential to break away from the common thermally activated transport. In the meantime, despite the advantages of a large-area production and suitability with numerous substrates,[14] vacuum-deposited small molecules sustain only a range of order on the microscopic scale, resulting in a lower probability of carriers crossing grain boundary in their mean free path and

Y. Zheng, T. Jiang, D. Zhu, L. Li, D. Ji
Tianjin Key Laboratory of Molecular Optoelectronic Sciences
Department of Chemistry
Institute of Molecular Aggregation Science
Tianjin University
Tianjin 300072, China
E-mail: jideyang@tju.edu.cn

Y. Zheng, W. Li
GPL Photonics Laboratory
State Key Laboratory of Applied Optics
Changchun Institute of Optics
Fine Mechanics and Physics
Chinese Academy of Sciences
Changchun 130033, China

The ORCID identification number(s) for the author(s) of this article can be found under https://doi.org/10.1002/adfm.202211742.

DOI: 10.1002/adfm.202211742

H. Lin
Suzhou Institute of Nano-Tech and Nano-Bionics
Chinese Academy of Sciences
Suzhou 215123, China

S. Qi
State Key Laboratory of Chemical Resource Engineering
Beijing University of Chemical Technology
Beijing 100029, China

W. Hu
Tianjin Key Laboratory of Molecular Optoelectronic Sciences
Department of Chemistry
School of Science
Tianjin University
Collaborative Innovation Center of Chemical Science and Engineering
Tianjin 300072, China
E-mail: huwp@tju.edu.cn

W. Hu
Joint School of National University of Singapore and Tianjin University
Fuzhou 350207, China

© 2022 Wiley-VCH GmbH

Check for updates
16163028, 0, Downloaded from https://onlinelibrary.wiley.com/doi/10.1002/adfm.202211742 by Cas-Changchun Institute Of Optics, Fine Mechanics And Physics, Wiley Online Library on [06/02/2023]. See the Terms and Conditions (https://onlinelibrary.wiley.com/terms-and-conditions) on Wiley Online Library for rules of use; OA articles are governed by the applicable Creative Commons License

not being trapped.[3,16,17] As a result, observing band-like transport in vacuum-deposited thin-film devices is more complicated. Besides that, there is no report about achieved band-like transport of vacuum-deposited thin-film on polymer dielectrics, which remains a difficult task due to the intricate internal and external impacts of the disrupted chain arrangement of polymer dielectrics.[4,17]

To a certain end, a simple bottom-up method of creating the buffer layer onto the solvent-resistant PI[24] is used to form a bi-polymer dielectric structure for the synergic effect of the growth and charge transport of organic semiconductors. The close association between the PI and buffer layer could significantly alter charge transport mechanism from thermally activated mode to band-like transport. Alternatively, the weak binding energy of the double-component dielectric materials only displays a thermally activated mode. In comparison, the single component of buffer layers, PI, and buffer layers/SiO_2, are also researched, which only show the action of the thermally activated mode. As a result, the bottom layer of PI plays the key point and shows the different binding capability with the upper dielectric layer, leading to the combination with strong interaction to tune the charge transport mechanism from thermally activated mode to band-like transport, providing a novel insight into the regulation of the polymer dielectric layer on the electronic properties of organic semiconductors.

2. Results and Discussion

Five common insulating polymers, including polystyrene (PS), polymethyl acrylate (PMMA), polyphenylene ether (PPO), polyacrylic acid (PAA), and poly(4-vinylphenol) (PVP) were opted. These were combined with solvent and low-temperature resistant PI for the formation of bilayer dielectrics (**Figure 1**a). In the current situation, interface was additionally modeled to evaluate the binding energy between dielectric layers (the details shown in supporting information) (Figure 1b). The binding energy of each complex model was listed in Table S1 (Supporting Information) and the histogram of binding energy per unit area (γ) (Figure 1c) represented the interface binding capability. With the elevation of a higher absolute value of γ, the interface binding capacity got stronger. Both the single-component dielectrics and buffer layers/PI displayed smooth surfaces with the root mean square (RMS) roughness of several angstroms as shown in Figure S1 and Table S2 (Supporting Information) from the atomic force microscope (AFM). Moreover, these five bilayer dielectrics showed different surface energies (Figure S2 and Table S3, Supporting Information). The introduction of the PI layer could further reduce the surface energy of its upper layers for the induction of better growth of semiconductors.

Based on these five systems, a simple and unique structured small molecule 2,6-diphenylanthracene (DPA) was opted as the active layer (Figure 1a). This molecule was selected due to its dense herringbone packing motif and multi-C-H-π interactions for effective charge transport.[25] DPA exhibited small-scale island-like growth on the surface of the bare PMMA and PPO, and then a layered structure with a larger size on the surface of PS, PAA and PVP (Figure S3, Supporting Information). Surprisingly, the DPA grown on the bare PI surface was extremely rough (Figure S4, Supporting Information), but PI, as the bottom layer of bilayer dielectrics, was able to not only improve the morphological characteristics of DPA with layer-by-layer structures (Figure S5, Supporting Information) but

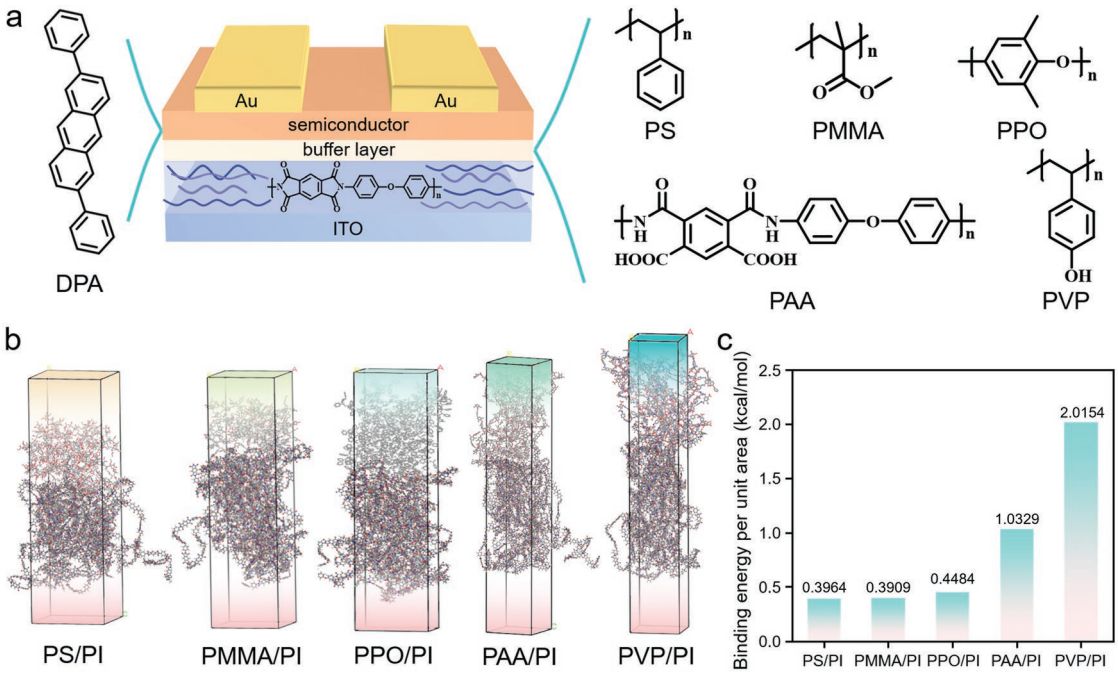

Figure 1. a) Schematic diagram of the bottom gate top contact OFET, the active layer is DPA (left), which serves as several polymers of the buffer layer (right). b) Modeling buffer layers/PI through Material Studio, and the dynamic simulation were completed by the Forcite module. c) The binding energy per unit area of the bilayer dielectric through Material Studio modeling.

© 2022 Wiley-VCH GmbH

16163028, 0, Downloaded from https://onlinelibrary.wiley.com/doi/10.1002/adfm.202211742 by Cas-Changchun Institute Of Optics, Fine Mechanics And Physics, Wiley Online Library on [06/02/2023]. See the Terms and Conditions (https://onlinelibrary.wiley.com/terms-and-conditions) on Wiley Online Library for rules of use; OA articles are governed by the applicable Creative Commons License

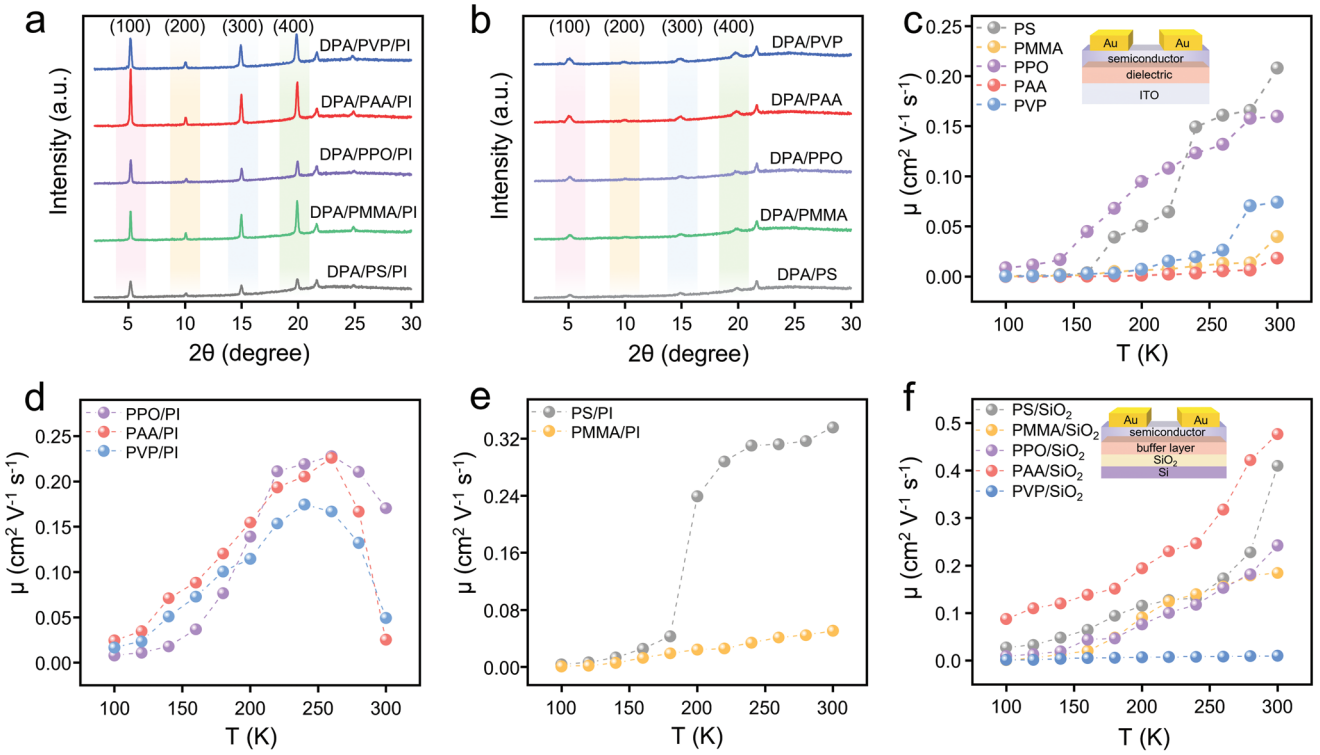

Figure 2. Out-of-plane XRD diffraction peaks of DPA grown on the surface of a) five double-component dielectrics and b) five single-component dielectrics. c) The carrier mobility (μ) of OFETs using these polymers as single-component dielectrics change with temperature and the schematic diagram of the device. Temperature-dependent carrier mobility in OFET based on d) PPO/PI, PAA/PI, PVP/PI dielectrics and e) PS/PI, PMMA/PI dielectrics. f) The changing trend of OFETs mobility of buffer layers/SiO_2 with temperature.

also improve the crystallinity and packing intensity of deposited films. The varying degrees of the roughness of DPA grown on the surface of different polymer dielectrics could be ascribed to different attributes. These attributes were the synergistic effects of the device interface that include the roughness, surface energy, and the role of interface functional groups of the dielectric layer. These particular characteristics directly affected the semiconductor stacking morphology and roughness.[1,2,11] The buffer layers/PI induced the growth of DPA toward a higher crystallinity (**Figure 2**a) compared to the single-component dielectrics (Figure 2b), as shown in out-of-plane X-ray diffraction (XRD) peaks of DPA on the different dielectrics. Furthermore, each crystal-plane exhibited narrow and sharp in-plane XRD diffraction peaks, and the magnitude of the peaks on the double-component dielectrics was generally higher than that of the single-component (Figure S6, Supporting Information).

Consequently, OFETs with the bottom-gate top-contact configuration was used to further investigate the charge transport of DPA on polymeric dielectrics. In particular, demonstrative p-type distribution and output features from single-component dielectric contrived OFETs (Figures S7 and S8, Supporting Information), were experienced with the mobility of around 0.001 $cm^2\ V^{-1}\ s^{-1}$ (PI), 0.06 $cm^2\ V^{-1}\ s^{-1}$ (PVP), 0.3 $cm^2\ V^{-1}\ s^{-1}$ (PS, PMMA, PPO), and 9 $cm^2\ V^{-1}\ s^{-1}$ (PAA) (Figure S9, Supporting Information). The vacuum variable temperature test established that only thermally activated mode was identified from these single-component dielectric layers. These layers showed a positive correlation between mobility and temperature ($d\mu/dT > 0$) not only for low mobility but also for highly mobile devices (Figure 2c; Figure S10, Supporting Information). This result could be further confirmed from the V_G-independence tendency of $d\mu/dT$ (Figure S11, Supporting Information) and temperature-independence capacitance (Figure S12, Supporting Information). The mobility was effectively increased by the order of 100 times of magnitude as compared with the bare PI dielectric layer (Figure S13, Supporting Information) when the PI opted as the bottom layer of the other five buffer layers (PS, PMMA, PPO, PAA, and PVP; Figure 1a). All of the devices with double-component dielectrics obtained the value of mobility around 0.1-0.3 $cm^2\ V^{-1}\ s^{-1}$ (Figures S14–S16, Supporting Information). Interestingly, PVP/PI, PAA/PI and PPO/PI based OFETs showed negative temperature coefficient of hole mobility ($d\mu/dT < 0$) for the presence of band-like transport from 300 to 260 K and positive temperature coefficient of hole mobility ($d\mu/dT > 0$) indicating the presence of thermally activated mode from 260 to 100 K (Figure 2d; Figure S17, Supporting Information). But for the devices with PS/PI and PMMA/PI dielectrics, there were still thermally activated mode from 300 to 100 K (Figure 2e). Furthermore, the mobility at various gate voltages (Figure S18, Supporting Information) was derived as a function of the temperature to remove the misinterpretation of the carrier system induced by gate-voltage dependence.[26] The thermal-independence capacity of double-component dielectrics (Figure S19, Supporting Information) could also ensure the deviation in the mobility calculation. Combined with the calculated binding energy of double-component dielectrics, it

© 2022 Wiley-VCH GmbH

16163028, 0, Downloaded from https://onlinelibrary.wiley.com/doi/10.1002/adfm.202211742 by Cas-Changchun Institute Of Optics, Fine Mechanics And Physics, Wiley Online Library on [06/02/2023]. See the Terms and Conditions (https://onlinelibrary.wiley.com/terms-and-conditions) on Wiley Online Library for rules of use; OA articles are governed by the applicable Creative Commons License

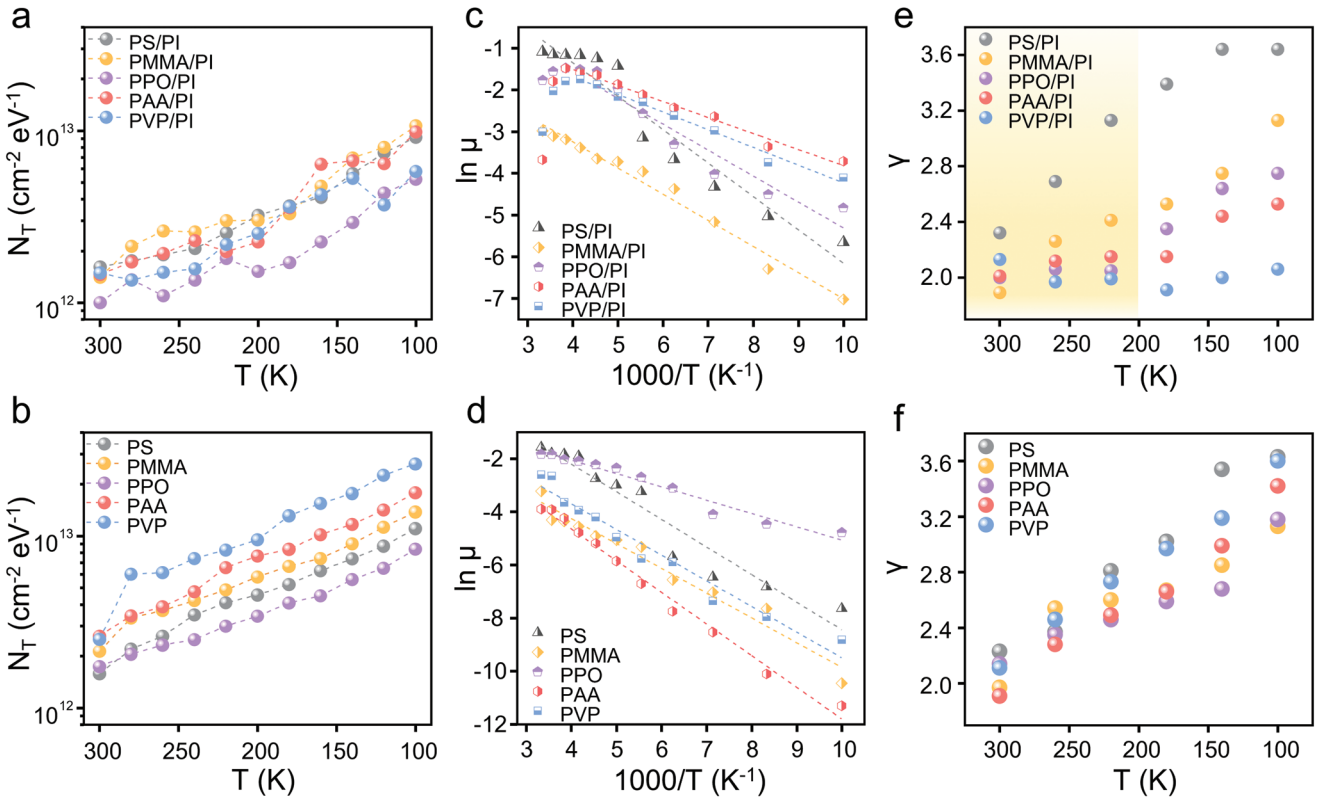

Figure 3. Temperature-dependent interface trap density (N_T) in OFETs with a) double and b) single-component dielectrics with the same upper surface. In the OFETs of c) double and d) single-component dielectrics, the activation energy (E_A) is extracted from the change of mobility with temperature. In these OFETs of e) double and f) single-component dielectrics, γ is plotted against T.

was discovered that the band-like transport mode occurred in the double-component dielectrics with the value of binding energy per unit area above 0.4 (PPO/PI, PAA/PI, and PVP/PI; Figure S20, Supporting Information).

Moreover, the limiting distribution transport was associated with the density of traps in various previous research.[4,12,17] According to the formula $N_T = \frac{C_i}{e}\left(\frac{eS}{ln10K_BT} - 1\right)$, the interface trap density (N_T) is as a function of temperature (T), where S is the sub-threshold swing, C_i is the capacitance per unit area, k_B is Boltzmann constant, and e is the basic charge. Noticeably, the N_T of single-module devices was greater as compared to double-component OFETs (**Figures 3**a,b; Figure S21, Supporting Information) for PPO, PAA, and PVP, which showed diverse distribution contrivances between single and double-component devices (Figure S20, Supporting Information). Congruently, for PS and PMMA that were thermally activated, the trap density for either single or double-component dielectric was only marginally diverse.

Moreover, the activation energy (E_A) was calculated to reflect the quality of the semiconductor layer and the magnitude of energy disorder at the interface.[11] According to $\mu = \mu_0 \, exp\left(-\frac{E_A}{K_BT}\right)$, where E_A is the activation energy, k_B is the Boltzmann constant. It was found that mobility decreased along with the decrease in temperature (Figure 3c). The E_A of the double-component dielectric OFETs, except the PPO and PPO/PI, was lesser than the single-component (Figure 3d and **Table 1**), which meant that the existence of the bottom PI could significantly regulate the growth of the active layer. Among them, the E_A of PAA/PI and PVP/PI were as less representing as 33.1 and 36.6 meV, respectively, which were nearer to the level of single-crystal OFETs in the past scientific reports (Table S4, Supporting Information).[11,12,14] The low value of E_A for single-component PPO devices possibly could be associated with its low-temperature resistance (e.g., brittle temperature in Table S5, Supporting Information).

Additionally, power-law exponent γ could further reflect the disorder energy of the system, which was calculated from the drain current (I_D) against the gate voltage (V_G) is at saturation. According to $I_D \propto (V_G - V_{th})^{\gamma}$,[27,28] it was found that in the temperature range of 220–300 K (band-like area) of PPO/PI, PAA/PI, and PVP/PI devices, they all vary in a narrow range with the thermal-independent value that was close to the ideal state (Figure 3e). This indicated the low disorder energy of these interfaces.[28] Compared to the disordered interfaces of

Table 1. The activation energy (E_A) of OFETs using different dielectrics.

	PS	PMMA	PPO	PAA	PVP
E_A/meV (buffer layer/PI)	69.1	54.07	54.79	33.12	36.60
E_A/meV (single-component)	89.83	80.56	49.87	102.90	83.45

© 2022 Wiley-VCH GmbH

16163028, 0, Downloaded from https://onlinelibrary.wiley.com/doi/10.1002/adfm.202211742 by Cas-Changchun Institute Of Optics, Fine Mechanics And Physics, Wiley Online Library on [06/02/2023]. See the Terms and Conditions (https://onlinelibrary.wiley.com/terms-and-conditions) on Wiley Online Library for rules of use; OA articles are governed by the applicable Creative Commons License

16163028, 0, Downloaded from https://onlinelibrary.wiley.com/doi/10.1002/adfm.202211742 by Cas-Changchun Institute Of Optics, Fine Mechanics And Physics, Wiley Online Library on [06/02/2023]. See the Terms and Conditions (https://onlinelibrary.wiley.com/terms-and-conditions) on Wiley Online Library for rules of use; OA articles are governed by the applicable Creative Commons License

PS/PI, PMMA/PI (Figure 3e), and single-component dielectric (Figure 3f) OFETs all displayed the upward trend as the temperature was reduced.[28] As a result, the introduction of PI modified the interface between the dielectrics (PPO, PPA, and PVP) and the semiconductor with high quality and low disorder energy, but had little effect on the PS and PMMA dielectric layers.

In order to verify the special bottom-up modulated effect of PI, 300 nm SiO_2 was used as the bottom dielectric to prepare the devices under the same conditions (Figure 2f; Figures S22–S24, Supporting Information). Although the buffer layers/SiO_2 interfaces had lesser E_A (Figure S25 and Table S6, Supporting Information) than single-component devices, the N_T (Figure S26, Supporting Information) and the power-law exponent γ (Figure S27, Supporting Information) nevertheless demonstrated increased disorder energy than the buffer layers/PI interfaces due to the high associated to temperature. In addition, the clear interface between the polymer and SiO_2 was observed from the scanning electron microscope (SEM) images as shown in Figure S28a–e. By comparison, the interface bonding capability between polymer buffer layers and PI was stronger due to the better compatibility without obvious interfaces (Figure S28f–j, Supporting Information). As a direct consequence, the presence of SiO_2 showed weak bottom-up modulation ability, resulting in all the thermally activated mode based on buffer layers/SiO_2 dielectrics. Such findings could support the notion that the synergism between the buffer layer and the PI was crucial for the regulation of the distribution of charge.

The low-temperature XRD measurements were performed on PS/PI and PVP/PI that with different charge transport mechanisms and their single-component dielectrics (**Figure 4**a; Figures S29 and S30, Supporting Information), and the findings were close to the altered trend of low-temperature mobility. It was discovered that the thermally activated mode represented the crystallinity of the semiconductor dropped significantly with the decrease of temperature (DPA with PS, PVP, and PS/PI), but the presence of band-like transport could boost the crystallinity first and then a slight decrease resulted with the temperature decrease, confirming the excellent performance of the interface (DPA with PVP/PI). The in-situ characteristic could demonstrate the alteration of the channel layer in the low temperature, and the distinction in the change tendency of the single/dual-dielectric also evidenced the impact of the bottom dielectric on the semiconductor layer.

The interaction in the dielectrics (PI and buffer layers) and semiconductors were then investigated using sum frequency generation vibrational spectroscopy (SFG-VS). SFG-VS is interface-selective technique that is sensitive to molecular ordering with broken central symmetry and physical features.[29–31] We have chosen PS/PI (Figures 4b,c) and PVP/PI (Figures 4e,f) and their single-component dielectrics for comparison studies at room and low temperature. At room temperature, there were no distinctive SFG peaks in the PS/ITO and PVP/ITO systems (Figures 4b,e), indicating that the polymer molecules were chains highly irregular. However, the introduction of PI caused the upper PS layer to order (crystallization), as evidenced by the presence of the distinctive feature SFG peak position of -CH_2 in the system of PS/PI/ITO (Figure 4b). In the meantime, the low temperature treatment would crystallize the PS layer, and the existence of PI could increase the degree of crystallization even further (Figure 4c). This type of polymeric crystal growth might be incongruent with the bottom PI layer, resulting in interface strain that was negative for the development and ordered the spatial organization of the organic semiconductor layer, thereby degrading electron transport. In contrast, no changes in the closer scrutiny of PVP/PI/ITO were observed at room and low temperatures after using the bottom layer of PI (Figure 4e,f) possibly due to the strong interface binding capacity of PVP and PI. Furthermore, at both room and low temperatures, a significant difference in non-resonant background was observed in these two types of OSC/PS/PI and OSC/PVP/PI systems. The decrease of non-resonant background in the OSC/PVP/PI system was seen to be much smaller as compared to the OSC/PS/PI system. Because the non-resonant background of SFG is closely connected to the built-in electric field caused by interfacial charge transport, the preceding observation showed that reasonably strong charge transfer between the semiconductor and the PVP/PI dielectric layer could lead to more effective charge transport.[32–35] As a result, it was determined that the bottom-up PVP/PI dielectric construction was well congruent as a "Lego-like" close combination (Figure 4g), which could efficaciously avoid interface stress and mediates charge carrier mobility. Misaligned interfaces, such as PS/PI (Figure 4d), would stimulate polymeric crystallization, causing interface pressure and obstructing charge transport.

Moreover, the density functional-based tight-binding (DFTB+) method[36,37] was used to examine the interaction between bilayer dielectrics and the bottom-up modulation mechanism. Highest occupied molecular orbital (HOMO) and lowest unoccupied molecular orbital (LUMO) of dielectric system was calculated first. According to our calculations, HOMO was dispersed in the upper layer PS (**Figure 5**a) or PVP (Figure 5c), while LUMO (Figure 5b,d) was dispersed in the bottom layer PI. Furthermore, the double-component dielectric was densely packed and had a comparatively tiny layer unevenly spaced, indicating that charge could be transmitted from the HOMO to the LUMO. A correlation of the HOMO and LUMO positions of the various materials indicated that the bilayer dielectric models had a smaller band gap value. In addition, from the data of partial density of state (PDOS) as shown in Figure S31 (Supporting Information), the distribution of p orbital states about PVP/PI was closer to the Fermi level and particularly had a continuous distribution in the –1 to 0 eV range[38] stating clearly that the excited state electrons were easier to transfer at the interface of PVP/PI than the PS/PI. Subsequently, the semiconductor/dielectric system was investigated further (Figure 5e–h), and it was discovered that the LUMO was still dispersed in the bottom layer PI, indicating the significance of the PI layer in bottom-up modulating DPA charge transport. As shown in Figure 5i, because of the p-electron orbitals of PVP continuously distributed around the Fermi energy level (–1 to 0 eV), the excited state electrons on PVP preferred to transfer to the empty electron orbitals of PI, leaving the holes on PVP to combine with the excited state electrons from DPA, which could be also confirmed by the PDOS between the pure PVP and DPA system (Figure S32a, Supporting Information). This charge transfer process would produce more holes in the

 © 2022 Wiley-VCH GmbH

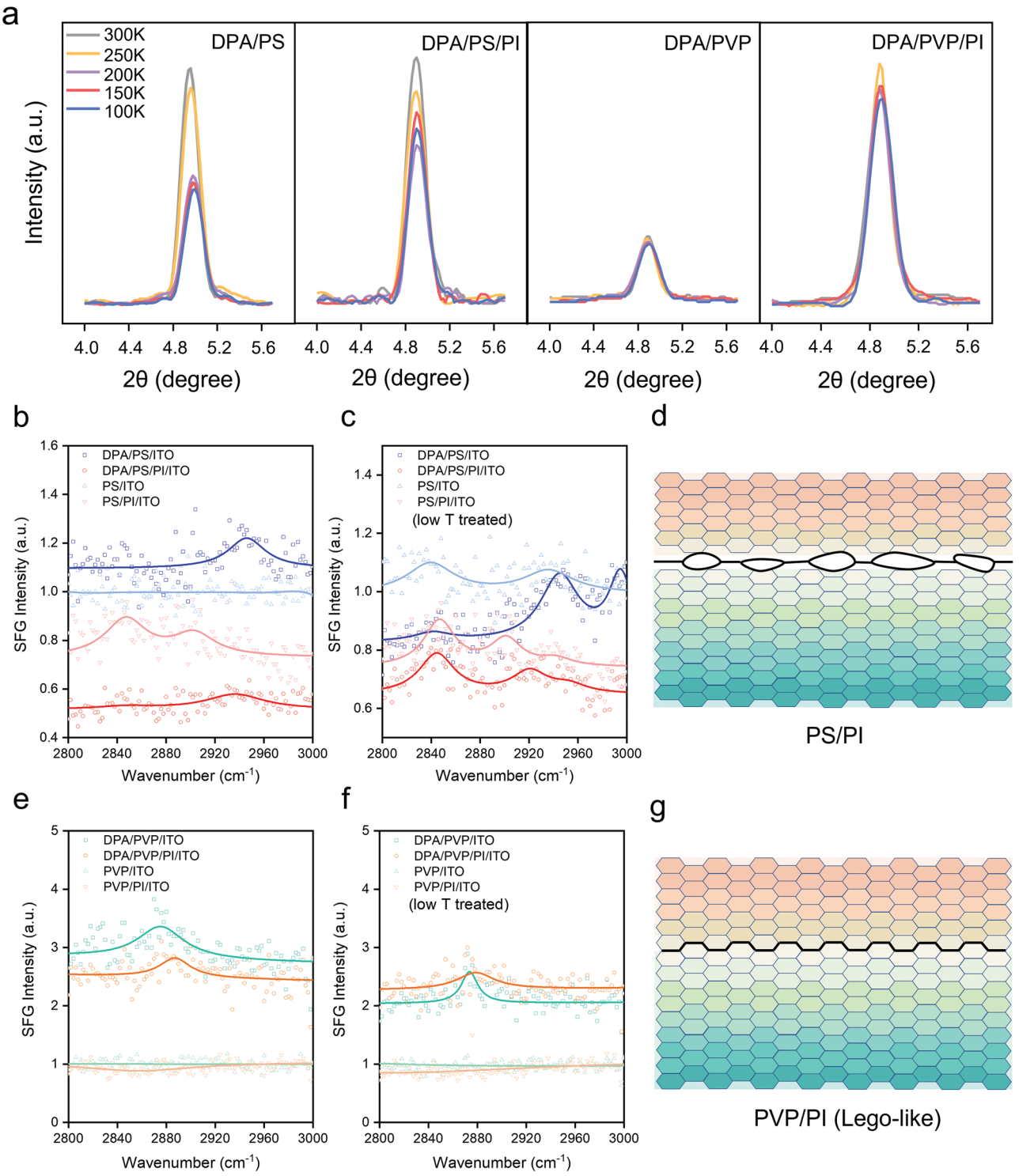

Figure 4. a) XRD diffraction peaks of (100) crystal plane of DPA films deposited on different dielectrics (PS, PS/PI, PVP, and PVP/PI) as a function of temperature. b) Sum frequency generation vibrational spectroscopy (SFG-VS) of PS single/double-component dielectrics and semiconductors on their surfaces, c) their SFG-VS after low-temperature treatment (liquid nitrogen). d) Schematic diagram of the interface between PS and PI. e) SFG-VS of PVP single/double-component dielectrics and semiconductors on their surfaces, f) their SFG-VS after low-temperature treatment (liquid nitrogen). g) A schematic diagram of a "Lego-like" combination between PVP and PI.

conduction channel for efficient charge transport. In contrast, in the DPA/PS/PI system (Figure 5j), there were fewer p-electron orbitals of PS distributed around the Fermi energy level (–1 to 0 eV), resulting in the difficult electron transfer process in this system. In addition, we also observed the excited state electrons preferred to transfer from PS to DPA (Figure S32b,

© 2022 Wiley-VCH GmbH

16163028, 0, Downloaded from https://onlinelibrary.wiley.com/doi/10.1002/adfm.202211742 by Cas-Changchun Institute Of Optics, Fine Mechanics And Physics, Wiley Online Library on [06/02/2023]. See the Terms and Conditions (https://onlinelibrary.wiley.com/terms-and-conditions) on Wiley Online Library for rules of use; OA articles are governed by the applicable Creative Commons License

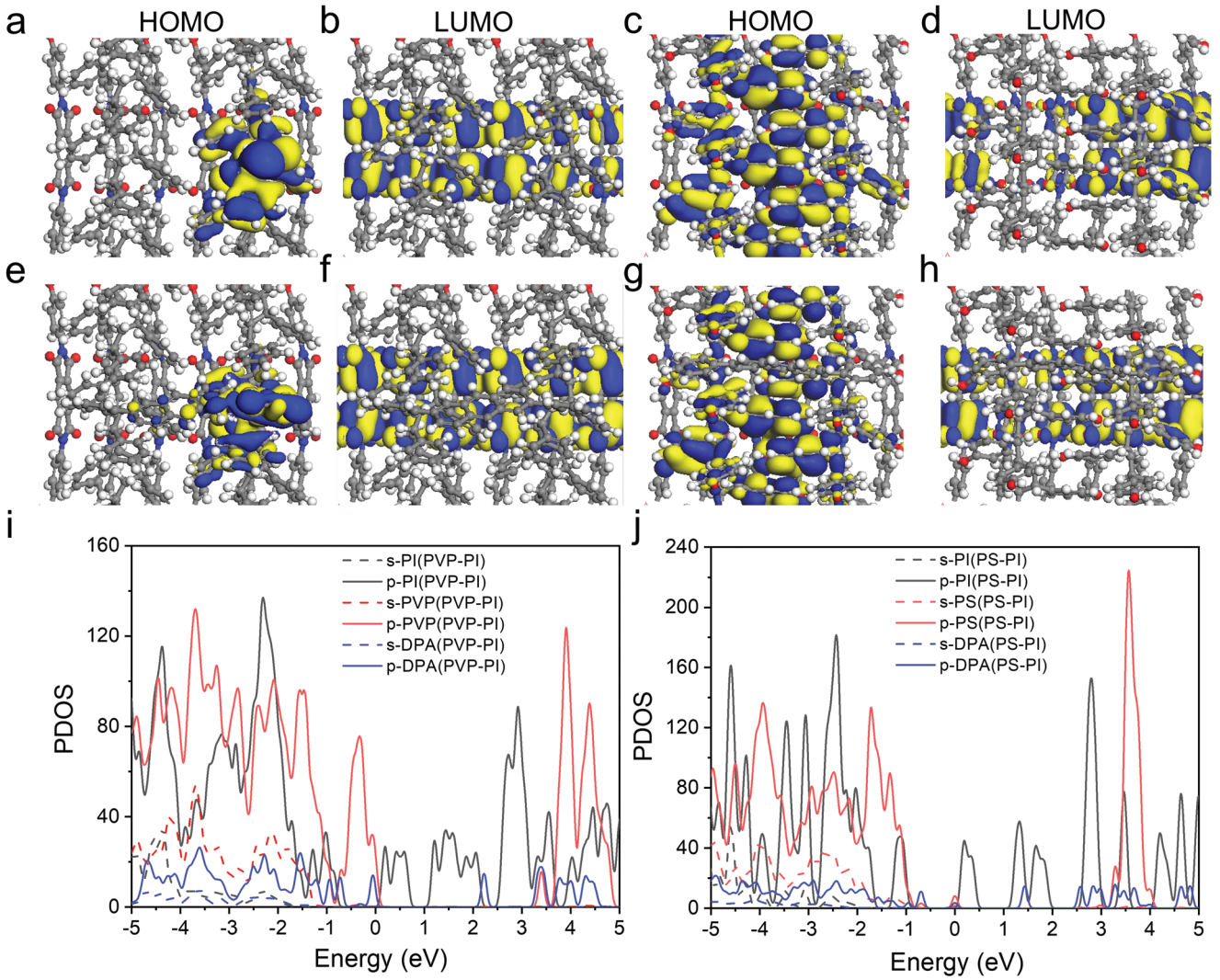

Figure 5. Density functional-based tight binding (DFTB+) calculation. The calculated HOMO of a) PS/PI, c) PVP/PI, e) DPA/PS/PI, g) DPA/PVP/PI. The calculated LUMO of b) PS/PI, d) PVP/PI, f) DPA/PS/PI, h) DPA/PVP/PI. Partial density of states (PDOS) of i) DPA/PVP/PI and j) DPA/PS/PI system.

Supporting Information), which was not conducive to charge transport. Hence, it could be summed up that PI could bottom-up regulate the distribution of charge of electrons among the semiconductor and dielectric layer for leaving more empty spaces and holes for effective distribution of charge at the DPA/PVP/PI interface.

3. Conclusion

In conclusion, an accomplishment in the band-like transport of small molecule thin film OFETs on polymer dielectrics was accomplished using the crucial concepts of the bottom-up construction method. We discovered that the binding energy in bilayer dielectrics was essential in attenuating charge transport, establishing an excellent framework for further research into the charge migration of polymer dielectrics and thin film device. Low-temperature XRD, AFM, theoretical calculations, and SFG-VS analysis revealed a "Lego-like" similar combination between PI and the upper PPO, PAA, and PVP, allowing the attenuation charge transport process from thermally activated mode to band-like transport to be recognized. Our findings offer new perspectives on the framework of study and performance optimization of small-molecule thin-film OFETs. It is extremely important cost-effective production of superior quality transistors on a large scale.

4. Experimental Section

ITO glass substrates used in the study were successively cleaned with deionized water, acetone, and pure ethanol, and then dried with nitrogen. O_2 plasma was used to treat the surface of ITO glass (50 W, 5 min). Diener electronic GmbH+Co.KG (Germany) was used to treat plasma in this case. We spin-coated the PI precursor (PAA) on the cleaned ITO glass at 3000 rpm before annealing it at 140 °C for 1 h and 300 °C for 2 h. PI has a thickness of 290 nm and a capacitive coupling of 10 nF cm^{-2}.

© 2022 Wiley-VCH GmbH

16163028, 0, Downloaded from https://onlinelibrary.wiley.com/doi/10.1002/adfm.202211742 by Cas-Changchun Institute Of Optics, Fine Mechanics And Physics, Wiley Online Library on [06/02/2023]. See the Terms and Conditions (https://onlinelibrary.wiley.com/terms-and-conditions) on Wiley Online Library for rules of use; OA articles are governed by the applicable Creative Commons License

After PI/SiO_2 was treated with O_2 plasma (50 W, 5 min), the buffer layer was acquired by spin coating with a 10 mg mL^{-1} solution of the polymer. All of the single-component dielectrics were formed by spin-coating on the ITO with a 50 mg mL^{-1} solution. Atomic Force Microscope was used to test the RMS of dielectric surface (Bruker Dimension Icon, USA). The static contact angle of the PI surface was measured by Pass LSA/OSA-100.

The surface energy is calculated according to the following formula: $1+\cos\theta = \frac{2(\gamma_s^d)^{\frac{1}{2}}(\gamma_l^d)^{\frac{1}{2}}}{\gamma_l} + \frac{2(\gamma_s^p)^{\frac{1}{2}}(\gamma_l^p)^{\frac{1}{2}}}{\gamma_l}$, where θ is the contact angle, γ_l is the liquid–gas surface tension, γ_l^d is the surface tension of the solid–liquid phase, γ_l^p is the polar surface tension of the liquid between the solid–liquid phase, and γ_s^d is the dispersed surface tension of the solid–liquid phase, γ_s^p is the polar surface tension of the solid between the solid–liquid phase.

Twenty nanometer DPA film was formed on the dielectric layer at rate of deposition of 0.05 Å s^{-1} and this scenario was achieved at a vacuum of 1×10^{-5} Pa. A metal mask was used to deposit 20 nm Au on the surface of the DPA at a deposition rate of 0.07 Å s^{-1} as source/drain electrodes. AFM images were recorded in tapping-mode utilizing a Bruker Dimension Icon microscope in atmospheric environment. In-plane and out-of-plane patterns of XRD were recorded by Rigaku SmartLab X-ray diffractometer with a power of 9 kW, a monochromatic radiation of Cu Kα (λ = 1.5406 Å), and a PB measurement mode. Low-temperature XRD was measured by Smartlab-9kw. The room-temperature electrical performance of the DPA FET was measured in the dark situation by using an Agilent B1500A semiconductor parameter analyzer. The mobility was extracted from the saturation region by using the equation of $I_{DS} = \left(\frac{W}{2L}\right) C_i \mu (V_G - V_T)^2$. The low-temperature test used a lakeshore low-temperature probe station equipped with a Keithley 2636 meter, and performed a variable temperature test in a vacuum of 3×10^{-4} Pa. Used PDA FS360 to measure the low- temperature capacitance of the insulating layer. Sum frequency generation (SFG) spectrometer laser system was built by EKSPLA, operating at 50 Hz with a copropagating configuration (SINANO, China), and the pulse width was ≈25 ps. The visible wavelength was fixed at 532 nm, while the IR rhythm was tunable between 1000 and 4300 cm^{-1}. The incident angle was 60° for the visible beam and 55° for the IR beam. The SFG signal was collected at around 59.5° in the reflection geometry within a small range depending on the IR wave number (2800 to 3000 cm^{-1} in the experiment). The spectrum was recorded at 2 cm^{-1} additions per scan and was around more than 200 laser pulses per point.

Supporting Information

Supporting Information is available from the Wiley Online Library or from the author.

Acknowledgements

The authors are grateful to National Key Research and Development Program of China (2021YFA0717900), National Natural Science Foundation of China (62004138, 52273190, 62134009, 62121005), Beijing National Laboratory for Molecular Sciences (BNLMS202006), the Haihe Laboratory of Sustainable Chemical Transformations, and Development Program of the Science and Technology of Jilin Province (20200802001GH).

Conflict of Interest

The authors declare no conflict of interest.

Data Availability Statement

The data that support the findings of this study are available from the corresponding author upon reasonable request.

Keywords

band-like transport, interface engineering, organic semiconductors, polymer dielectrics, thin-film transistors

Received: October 10, 2022
Revised: December 5, 2022
Published online:

[1] H. L. Chen, W. N. Zhang, M. L. Li, G. He, X. F. Guo, *Chem. Rev.* **2020**, *120*, 2879.
[2] T. Yokota, T. Kajitani, R. Shidachi, T. Tokuhara, M. Kaltenbrunner, Y. Shoji, F. Ishiwari, T. Sekitani, T. Fukushima, T. Someya, *Nat. Nanotech.* **2018**, *13*, 139.
[3] H. Sirringhaus, *Adv. Mater.* **2014**, *26*, 1319.
[4] S, F. , M. Nikolka, A. Salleo, G. Schweicher, H. Sirringhaus, *Nat. Mater.* **2020**, *19*, 491.
[5] Y. N. Huang, X. Gong, Y. C. Meng, Z. W. Wang, X. S. Chen, J. Li, D. Y. Ji, Z. M. Wei, L. Q. Li, W. P. Hu, *Nat. Commun.* **2021**, *12*, 21.
[6] M. Y. Sun, C. C. Zhang, D. Chen, J. Wang, Y. C. Ji, N. Liang, H. Y. Gao, S. S. Cheng, H. Liu, *SmartMat.* **2021**, *2*, 213.
[7] K. K. Zhou, K. Dai, C. T. Liu, C. Y. Shen, *SmartMat.* **2020**, *1*, e1010.
[8] V. Coropceanu, J. Cornil, D. A. S. Filho, Y. Olivier, R. Silbey, J. L. Brédas, *Chem. Rev.* **2007**, *107*, 926.
[9] J. M. Cho1, T. Higashino1, T. Mori, *Appl. Phys. Lett.* **2015**, *106*, 193303.
[10] S. Kumagai, S. Watanabe, H. Ishii, N. Isahaya, A. Yamamura, T. Wakimoto, H. Sato, A. Yamano, T. Okamoto, J. Takeya, *Adv. Mater.* **2020**, *32*, 2003245.
[11] Y. J. Shi, L. Jiang, J. Liu, Z. Y. Tu, Y. Y. Hu, Q. H. Wu, Y. P. Yi, E. Gann, C. R. McNeill, H. X. Li, W. P. Hu, D. B. Zhu, H. Sirringhaus, *Nat. Commun.* **2018**, *9*, 2933.
[12] T. He, Y. F. Wu, G. D'Avino, E. Schmidt, M. Stolte, J. Cornil, D. Beljonne, P. P. Ruden, F. Würthner, C. D. Frisbie, *Nat. Commun.* **2018**, *9*, 2141.
[13] T. He, M. Stolte, Y. Wang, R. Renner, P. P. Ruden, F. Würthner, C. D. Frisbie, *Nat. Mater.* **2021**, *20*, 1532.
[14] I. N. Hulea, S. Fratini, H. Xie, C. L. Mulder, N. N. Iossad, G. Rastelli, S. Ciuchi, A. F. Morpurgo, *Nat. Mater.* **2006**, *5*, 982.
[15] M. A. Stoeckel, Y. Olivier, M. Gobbi, D. Dudenko, V. Lemaur, M. Zbiri, A. A. Y. Guilbert, G. D'Avino, F. Liscio, A. Migliori, L. Ortolani, N. Demitri, X. Jin, Y. G. Jeong, A. Liscio, M. V. Nardi, L. Pasquali, L. Razzari, D. Beljonne, P. Samorì, E. Orgiu, *Adv. Mater.* **2021**, *33*, 2007870.
[16] N. A. Minder, S. Ono, Z. H. Chen, A. Facchetti, A. F. Morpurgo, *Adv. Mater.* **2012**, *24*, 503.
[17] Y. C. Mei, P. J. Diemer, M. R. Niazi, R. K. Hallan, K. Jarolimek, C. S. Day, C. Risko, J. E. Anthony, A. Amassian, O. D. Jurchescu, *Proc. Natl. Acad. Sci U. S. A.* **2017**, *33*, E6739.
[18] T. Sakanoue, H. Sirringhaus, *Nat. Mater.* **2010**, *9*, 736.
[19] A. D. Scaccabarozzi, F. Scuratti, A. J. Barker, A. Basu, A. F. Paterson, Z. P. Fei, O. Solomeshch, A. Petrozza, N. Tessler, M. Heeney, T. D. Anthopoulos, M. Caironi, *Adv. Electron. Mater.* **2020**, *6*, 2000539.
[20] B. Y. Peng, S. Y. Huang, Z. W. Zhou, P. K. L. Chan, *Adv. Funct. Mater.* **2017**, *27*, 1700999.

© 2022 Wiley-VCH GmbH

16163028, 0, Downloaded from https://onlinelibrary.wiley.com/doi/10.1002/adfm.202211742 by Cas-Changchun Institute Of Optics, Fine Mechanics And Physics, Wiley Online Library on [06/02/2023]. See the Terms and Conditions (https://onlinelibrary.wiley.com/terms-and-conditions) on Wiley Online Library for rules of use; OA articles are governed by the applicable Creative Commons License

[21] J. Lee, J. W. Chung, D. H. Kim, B. L. Lee, J. Park, S. Lee, R. Häusermann, B. Batlogg, S. Lee, I. Choi, I. W. Kim, M. S. Kang, *J. Am. Chem. Soc.* **2015**, *137*, 7990.
[22] A. Luzio, F. Nübling, J. Martin, D. Fazzi, P. Selter, E. Gann, C. R. McNeill, M. Brinkmann, M. R. Hansen, N. Stingelin, M. Sommer, M. Caironi, *Nat. Commun.* **2019**, *10*, 3365.
[23] S. Schott, E. Gann, L. Thomsen, S. H. Jung, J. K. Lee, C. R. McNeill, H. Sirringhaus, *Adv. Mater.* **2015**, *27*, 7356.
[24] D. Y. Ji, T. Li, W. P. Hu, H. Fuchs, *Adv. Mater.* **2019**, *31*, 1806070.
[25] J. Liu, H. T. Zhang, H. L. Dong, L. Q. Meng, L. F. Jiang, L. Jiang, Y. Wang, J. S. Yu, Y. M. Sun, W. P. Hu, A. J. Heeger, *Nat. Commun.* **2015**, *6*, 10032.
[26] T. Z. Yang, Q. Wu, F. H. Dai, K. R. Huang, H. H. Xu, C. N. Liu, C. D. Chen, S. J. Hu, X. C. Liang, X. Y. Liu, Y. Y. Noh, C. Liu, *Adv. Funct. Mater.* **2019**, *30*, 1903889.
[27] D. Venkateshvaran, M. Nikolka, A. Sadhanala, V. Lemaur, M. Zelazny, M. Kepa, M. Hurhangee, A. J. Kronemeijer, V. Pecunia, I. Nasrallah, I. Romanov, K. Broch, I. McCulloch, D. Emin, Y. Olivier, J. Cornil, D. Beljonne, H. Sirringhaus, *Nature* **2014**, *515*, 384.
[28] J. J. Brondijk, W. S. C. Roelofs, S. G. J. Mathijssen, A. Shehu, T. Cramer, F. Biscarini, P. W. M. Blom, D. M. Leeuw, *Phys. Rev. Lett.* **2012**, *109*, 056601.
[29] P. G. Sionnest, J. H. Hunt, Y. R. Shen, *Phys. Rev. Lett.* **1987**, *59*, 1597.
[30] Y. R. Shen, *Nature* **1989**, *337*, 519.
[31] Z. W. Wang, H. Z. Lin, X. Zhang, J. Li, X. S. Chen, S. G. Wang, W. B. Gong, H. Yan, Q. Zhao, W. B. Lv, X. Gong, Q. B. Xiao, F. J. Li, D. Y. Ji, X. T. Zhang, H. L. Dong, L. Q. Li, W. P. Hu, *Sci. Adv.* **2021**, *7*, eabf8555.
[32] H. K. Ye, A. A. Akeel, J. Huang, H. E. Katz, D. H. Gracias, *J. Am. Chem. Soc.* **2006**, *128*, 6528.
[33] T. C. Anglin, Z. Sohrabpour, A. M. Massar, *J. Phys. Chem. C* **2011**, *115*, 20258.
[34] T. C. Anglin, J. C. Speros, A. M. Massari, *J. Phys. Chem. C* **2011**, *115*, 16027.
[35] S. R. Walter, J. Youn, J. D. Emery, S. Kewalramani, J. W. Hennek, M. J. Bedzyk, A. Facchetti, T. J. Marks, F. M. Geiger, *J. Am. Chem. Soc.* **2012**, *134*, 11726.
[36] B. Hourahine, B. Aradi, V. Blum, F. Bonafé, A. Buccheri, C. Camacho, C. Cevallos, M. Y. Deshaye, T. Dumitrică, A. Dominguez, S. Ehlert, M. Elstner, T. van der Heide, J. Hermann, S. Irle, J. J. Kranz, C. Köhler, T. Kowalczyk, T. Kubař, I. S. Lee, V. Lutsker, R. J. Maurer, S. K. Min, I. Mitchell, C. Negre, T. A. Niehaus, A. M. N. Niklasson, A. J. Page, A. Pecchia, G. Penazzi, et al., *J. Chem. Phys.* **2020**, *152*, 124101.
[37] M. Gaus, A. Goez, M. Elstner, *J. Chem. Theory Comput.* **2013**, *9*, 338.
[38] W. Zheng, Q. Liu, Z. G. Lu, *Chuneng Kexue Yu Jishu* **2020**, *9*, 1416.

© 2022 Wiley-VCH GmbH

16163028, 0, Downloaded from https://onlinelibrary.wiley.com/doi/10.1002/adfm.202211742 by Cas-Changchun Institute Of Optics, Fine Mechanics And Physics, Wiley Online Library on [06/02/2023]. See the Terms and Conditions (https://onlinelibrary.wiley.com/terms-and-conditions) on Wiley Online Library for rules of use; OA articles are governed by the applicable Creative Commons License